


Acoustically Excited Magnetic Dynamics and Spin Flow in Spin-Valve Structures

Andrei V. Azovtsev* and Nikolay A. Pertsev[✉]

Ioffe Institute, St. Petersburg 194021, Russia

 (Received 10 October 2021; revised 2 February 2022; accepted 11 March 2022; published 29 March 2022)

Acoustic waves and strain pulses created by a piezoelectric or optical transducer represent an attractive tool for the generation of spin dynamics in magnetoelastic materials and heterostructures. The advantage of acoustic excitation consists in much lower power consumption compared with the classical excitation by a microwave magnetic field. The magnetization precession driven by elastic waves can be further used for spin pumping into normal metals and semiconductors. Here we describe theoretically the magnetization dynamics and spin flow induced by plane acoustic waves traversing trilayer structures involving two ferromagnetic (F) films separated by a layer of normal metal (N). The problem is solved by advanced micromagnetoelastic simulations, which allow for the two-way coupling between spins and strains in the F films and their long-range dynamic interaction resulting from the spin flow across the N spacer. To derive the expression for such an interaction, we solve the spin-diffusion equation in N with the account of spin pumping created by dynamically strained F films and spin backflow through the interfaces. Performing numerical simulations for the $\text{Fe}_{81}\text{Ga}_{19}/\text{Au}/\text{Fe}_{81}\text{Ga}_{19}$ trilayers excited by longitudinal and transverse elastic waves, we quantify the inhomogeneous magnetization precession in the galfenol films and determine the spatial distributions of the oscillating spin current and spin accumulation in the Au spacers of different thickness. These distributions are further used to calculate the mean spin current and total spin accumulation in the spacer. It is found that both ac and dc parts of these quantities exhibit strong variations with the spacer thickness. Remarkably, the nonzero components of the total spin accumulation and mean spin current mostly have pronounced maxima at Au thicknesses amounting to about 0.25 and 0.75 of the wavelength λ_N of the elastic wave in Au, which is explained by an analytical model of strain distribution in the trilayer. Our theoretical results, which shed light on the acoustically excited generation of spin imbalance in magnetoelastic spin-valve structures, could be useful for the development of energy-efficient spin injectors into normal conductors with weak spin-flip scattering.

DOI: [10.1103/PhysRevApplied.17.034070](https://doi.org/10.1103/PhysRevApplied.17.034070)

I. INTRODUCTION

Metallic multilayers consisting of alternating ferromagnetic and nonmagnetic films represent a type of heterostructure, which is famous for the phenomenon of giant magnetoresistance (GMR) [1,2]. The simplest form of such a heterostructure is a spin valve comprising two ferromagnetic (F) films separated by a layer of normal metal (N). Owing to the GMR effect, F/N multilayers and spin valves can be employed as sensors of magnetic fields [3,4], which was implemented in magnetoresistive read heads of hard-disk drives [5,6]. Magnetic random access memories based on spin valves exhibiting non-volatile resistive switching can be developed as well [7–9]. Recently, it was shown that the use of spin valves renders it possible to increase the output power of spin-orbit torque nano-oscillators, which represent current-controlled compact sources of microwave signals [10].

At nanoscale thicknesses of the N interlayer, the F films in the spin valve are coupled by the static short-range Ruderman-Kittel-Kasuya-Yosida (RKKY) oscillatory exchange [11,12]. A long-range dynamic interaction between F films also appears in spin valves subjected to microwave magnetic fields, where the film magnetizations experience precessional motions [13]. This exchange coupling is caused by nonequilibrium spin currents generated in the N interlayer owing to the spin pumping by the adjacent precessing ferromagnets [14]. However, aside from the microwave field, the magnetization precession can also be excited by laser radiation [15], acoustic waves and strain pulses acting on magnetoelastic materials [16–21], electric currents [22,23], and microwave voltages applied to nanostructures with electric-field-controlled magnetic anisotropy [24–26]. Thus, the dynamic exchange coupling mediated by the spin flow in the N spacer may appear in $F/N/F$ heterostructures subjected to various external stimuli, as revealed recently in pseudospin valves excited by femtosecond laser pulses [27].

*azovtsev@mail.ioffe.ru

The dynamic coupling influences the magnetization precession in the F films via a torque created by the pumped spin current crossing the N spacer with a weak spin-flip scattering [13]. In $F/N/F$ trilayers subjected to a microwave magnetic field, this torque manifests itself in a change of the linewidth of ferromagnetic resonance (FMR) [13]. When the F layers have the same resonance frequency and parallel magnetizations, the FMR linewidth reduces drastically in comparison with that of the uncoupled F layers, because the overall spin current in the spacer vanishes [13]. In contrast, the FMR linewidth increases in spin valves with antiparallel magnetizations, where the spin currents pumped by two F layers add to each other [28,29]. Hence, suitable $F/N/F$ trilayers could be more efficient spin injectors into normal metals than the F/N bilayers [29,30]. Recently, it was shown that the dynamic coupling also affects the decay rates of the magnetization precessions launched by femtosecond laser pulses in the $\text{Fe}_{81}\text{Ga}_{19}/\text{Cu}/\text{Fe}_{81}\text{Ga}_{19}$ pseudospin valve [27].

In this work, we theoretically study the acoustically driven dynamics of spin-valve structures comprising the F films with a strong magnetoelastic coupling between spins and strains and the N interlayer with a weak spin-flip scattering. Our approach is based on the numerical modeling of the coupled magnetic and elastic dynamics in ferromagnetic heterostructures [31–33]. We consider $F1/N/F2$ trilayers dynamically strained by plane longitudinal and transverse elastic waves, which can be generated by a piezoelectric or optical transducer attached to one of the F films (Fig. 1). Numerical simulations are performed for $\text{Fe}_{81}\text{Ga}_{19}/\text{Au}/\text{Fe}_{81}\text{Ga}_{19}$ trilayers traversed by monochromatic acoustic waves with the frequency providing an efficient excitation of the magnetization precession in the galphenol films. The simulations take into account the spin flow in the Au spacer, which is generated by

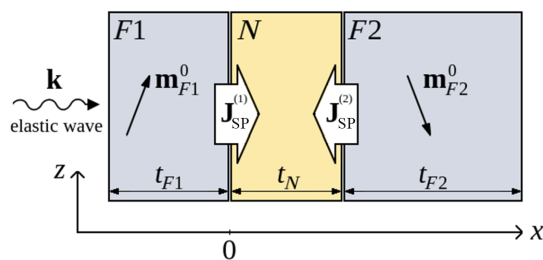


FIG. 1. Schematic representation of the spin-valve structure comprising two ferromagnetic films $F1$ and $F2$ and a normal-metal spacer N . The elastic wave is injected into $F1$ and then propagates across the structure, inducing inhomogeneous magnetization dynamics in ferromagnetic films. The magnetization precession at two F/N interfaces leads to spin pumping into the N layer. The unit vectors \mathbf{m}_{F1}^0 and \mathbf{m}_{F2}^0 show the equilibrium magnetization directions in $F1$ and $F2$. The projections of these vectors on the z axis may have either opposite or the same sign.

the dynamically strained $\text{Fe}_{81}\text{Ga}_{19}$ films, and the resulting dissipative coupling of the magnetization precessions occurring in two F films.

The paper is organized as follows. Section II is dedicated to theoretical description of the magnetoelastic dynamics in $F1/N/F2$ trilayers, Sec. III discusses the results of the simulations of elastic wave propagation across $\text{Fe}_{81}\text{Ga}_{19}/\text{Au}/\text{Fe}_{81}\text{Ga}_{19}$ trilayers, Sec. IV provides the summary of the work, and Appendix delivers the analysis of the strain distribution in the studied heterostructure in order to explain the results of the simulations.

II. MODELING OF MAGNETOELASTIC DYNAMICS IN $F1/N/F2$ TRILAYERS

The simulations are performed using a unified ensemble of nanoscale computational cells covering the whole $F1/N/F2$ trilayer. The magnetization dynamics inside the $F1$ and $F2$ films is described by the standard Landau-Lifshitz-Gilbert (LLG) equation [32] written for the unit vector $\mathbf{m}(\mathbf{r}, t)$ defining the magnetization direction in the F cells. Variations of the mechanical displacement $\mathbf{u}(\mathbf{r}, t)$ in the trilayer are quantified by the elastodynamic equation of motion [32]. The two-way coupling between the magnetization and strain in F layers is accounted for via a magnetoelastic contribution to the effective field \mathbf{H}_{eff} involved in the LLG equation and by adding magnetoelastic terms to the elastodynamic equation [32]. The effective field \mathbf{H}_{eff} acting on the magnetization also includes other relevant contributions, which result from the external magnetic field \mathbf{H} , exchange coupling, cubic magnetocrystalline anisotropy, and dipolar interaction between the spins [34]. Hence, our simulations take into account the magnetostatic interaction between the F films, but ignore the RKKY coupling because it is negligible at the considered spacer thicknesses $t_N > 20$ nm.

The dynamic exchange coupling between the F layers gives rise to additional terms in the LLG equation, which describe the torque created by the spin flow across the N layer [13]. Since the spin momentum orthogonal to the magnetization cannot penetrate into three-dimensional (3D) metals beyond the spin-coherence length of less than 1 nm [35], this torque should be introduced only in the computational cells adjacent to the $F1/N$ and $F2/N$ interfaces. In order to obtain the expression for such a torque in an explicit form, we solve the spin-diffusion equation in the N layer, which operates with the spin accumulation $\boldsymbol{\mu}_s(x, t)$. This vector quantity represents a nonequilibrium chemical potential imbalance defined by the relation $\boldsymbol{\mu}_s \equiv \int d\epsilon \text{Tr}[\hat{\sigma} \hat{f}(\epsilon)]$, where $\hat{\sigma}$ is the Pauli matrix vector, and $\hat{f}(\epsilon)$ is the 2×2 matrix distribution function at a given energy ϵ in the N layer [36]. In the adiabatic approximation, the spin-diffusion equation governing the spatial distribution of spin imbalance across the spacer can be

written as [36]

$$\frac{\partial \boldsymbol{\mu}_s}{\partial t} = D \frac{\partial^2 \boldsymbol{\mu}_s}{\partial x^2} - \frac{\boldsymbol{\mu}_s}{\tau_{\text{SF}}}, \quad (1)$$

where D is the diffusion coefficient and τ_{SF} is the spin-flip relaxation time. An adiabatic approximation implies that the magnetization precesses around its equilibrium direction slowly on the time scale of electronic relaxation in the F/N system, and at each time moment the system can be considered to be in a steady state. In order for this approximation to apply, the angular frequency $2\pi\nu$ of the magnetization precession should be well below the spin-flip rate τ_{SF}^{-1} in N [36]. For the studied $\text{Fe}_{81}\text{Ga}_{19}/\text{Au}$ system, the spin-flip relaxation time τ_{SF} is about 10 ps [37], and the maximal value of $2\pi\nu$ in our simulations amounts to about 36 GHz, which is significantly smaller than $\tau_{\text{SF}}^{-1} \sim 100$ GHz, justifying the use of the spin-diffusion equation in the form of Eq. (1). The spin accumulation $\boldsymbol{\mu}_s$ determines the spin-current density \mathbf{J}_s , which is a second-rank

tensor characterizing the direction of spin flow and the orientation and magnitude of the carried spin polarization per unit volume [38]. In our one-dimensional model, the density \mathbf{J}_s is defined by the relation $\mathbf{e}_n \cdot \mathbf{J}_s(x, t) = -[\sigma \hbar / (4e^2)] \partial \boldsymbol{\mu}_s(x, t) / \partial x$, where \mathbf{e}_n is the unit vector normal to the interface and pointing into the N layer, e is the elementary positive charge, and σ is the electrical conductivity of the N layer. The boundary condition for \mathbf{J}_s at the F/N interfaces reads $\mathbf{J}_s = \mathbf{J}_{\text{SP}} + \mathbf{J}_{\text{SB}}$, where the density \mathbf{J}_{SP} of the pumped spin current can be evaluated via the approximate relation $\mathbf{e}_n \cdot \mathbf{J}_{\text{SP}} \simeq (\hbar/4\pi) \text{Re}[g_{\uparrow\downarrow}^r] \mathbf{m} \times \dot{\mathbf{m}}$, $\mathbf{J}_{\text{SB}}(x, t)$ is the density of the spin backflow defined by the formula $\mathbf{e}_n \cdot \mathbf{J}_{\text{SB}} \approx -\text{Re}[g_{\uparrow\downarrow}^r] \boldsymbol{\mu}_s / 4\pi$, \hbar is Planck's constant, and $\text{Re}[g_{\uparrow\downarrow}^r]$ is the real part of the complex reflection spin-mixing conductance per unit area of the F/N contact [39]. The solution of Eq. (1) yields the following expressions for the spin accumulation $\boldsymbol{\mu}_s(x, t)$ and spin current $J_{xi}^s(x, t)$ flowing along the x axis in the spacer ($i = x, y, z$):

$$\begin{aligned} \mu_i^s(x, t) &= \frac{4e^2 \lambda_{\text{SD}} J_{xi}^{\text{SP}(1)}(t) \left[\cosh\left(\frac{tN-x}{\lambda_{\text{SD}}}\right) + \eta_2 \sinh\left(\frac{tN-x}{\lambda_{\text{SD}}}\right) \right] - J_{xi}^{\text{SP}(2)}(t) \left[\cosh\left(\frac{x}{\lambda_{\text{SD}}}\right) + \eta_1 \sinh\left(\frac{x}{\lambda_{\text{SD}}}\right) \right]}{\sigma \hbar \sinh\left(\frac{tN}{\lambda_{\text{SD}}}\right) \left[1 + (\eta_1 + \eta_2) \coth\left(\frac{tN}{\lambda_{\text{SD}}}\right) + \eta_1 \eta_2 \right]}, \\ J_{xi}^s(x, t) &= \frac{J_{xi}^{\text{SP}(1)}(t) \left[\sinh\left(\frac{tN-x}{\lambda_{\text{SD}}}\right) + \eta_2 \cosh\left(\frac{tN-x}{\lambda_{\text{SD}}}\right) \right] + J_{xi}^{\text{SP}(2)}(t) \left[\sinh\left(\frac{x}{\lambda_{\text{SD}}}\right) + \eta_1 \cosh\left(\frac{x}{\lambda_{\text{SD}}}\right) \right]}{\sinh\left(\frac{tN}{\lambda_{\text{SD}}}\right) \left[1 + (\eta_1 + \eta_2) \coth\left(\frac{tN}{\lambda_{\text{SD}}}\right) + \eta_1 \eta_2 \right]}, \end{aligned} \quad (2)$$

where

$$\begin{aligned} \mathbf{e}_x \cdot \mathbf{J}_{\text{SP}}^{(1)}(t) &= \frac{\hbar}{4\pi} \text{Re}[g_{\uparrow\downarrow}^{r(1)}] \mathbf{m}_1 \times \dot{\mathbf{m}}_1, \\ \mathbf{e}_x \cdot \mathbf{J}_{\text{SP}}^{(2)}(t) &= -\frac{\hbar}{4\pi} \text{Re}[g_{\uparrow\downarrow}^{r(2)}] \mathbf{m}_2 \times \dot{\mathbf{m}}_2, \end{aligned} \quad (3)$$

\mathbf{e}_x is the unit vector in the direction of the x axis, \mathbf{m}_1 and \mathbf{m}_2 define the magnetization orientations in the cells adjacent to the $F1/N$ and $F2/N$ interfaces, respectively, λ_{SD} is the spin-diffusion length in the N layer (taken equal to 35 nm [40] in our simulations of $\text{Fe}_{81}\text{Ga}_{19}/\text{Au}/\text{Fe}_{81}\text{Ga}_{19}$ trilayers), and $\eta_{1,2} = e^2 \text{Re}[g_{\uparrow\downarrow}^{r(1,2)}] \lambda_{\text{SD}} / (\sigma \hbar \pi)$ are the dimensionless quantities characterizing the two F/N contacts. Equations (2) represent a useful result, because they

describe the distributions of spin accumulation and spin current in a normal metal or semiconductor layer with spin pumping from both sides and the account of spin backflow. If the spin pumping from either side is absent, the corresponding $J_{xi}^{\text{SP}}(t)$ can be set to zero, and if one wishes to disregard the spin backflow through one of the interfaces, the corresponding η should be set to zero, yielding familiar formulas present in the literature.

The derived expression for $J_{xi}^s(x, t)$ enabled us to generalize the results of Refs. [13] and [36] and obtain the modified LLG equation for the unit vectors \mathbf{m}_k in computational cells adjacent to the $F1/N$ and $F2/N$ interfaces in the form (subscripts k and l take values 1, 2, which correspond to films $F1$ and $F2$; when $k = 1, l = 2$, and vice versa)

$$\frac{d\mathbf{m}_k}{dt} = -\frac{\gamma}{1 + (\alpha_k + \alpha'_k)^2} \left[\mathbf{m}_k \times \mathbf{H}_{\text{eff}}^{(k)} + (\alpha_k + \alpha'_k) \mathbf{m}_k \times \mathbf{m}_k \times \mathbf{H}_{\text{eff}}^{(k)} - \alpha'_k \mathbf{m}_l \times \mathbf{m}_l \times \mathbf{H}_{\text{eff}}^{(l)} \right];$$

$$\alpha'_k = \frac{\gamma \hbar \text{Re}[g_{\uparrow\downarrow}^{r(k)}] \left[\sinh\left(\frac{t_N}{\lambda_{SD}}\right) + \eta_l \cosh\left(\frac{t_N}{\lambda_{SD}}\right) \right]}{4\pi M_s^{(k)} \Delta x \sinh\left(\frac{t_N}{\lambda_{SD}}\right) \left[1 + (\eta_k + \eta_l) \coth\left(\frac{t_N}{\lambda_{SD}}\right) + \eta_k \eta_l \right]}, \quad (4)$$

$$\alpha''_k = \frac{\gamma \hbar \text{Re}[g_{\uparrow\downarrow}^{r(l)}] \eta_k}{4\pi M_s^{(k)} \Delta x \sinh\left(\frac{t_N}{\lambda_{SD}}\right) \left[1 + (\eta_k + \eta_l) \coth\left(\frac{t_N}{\lambda_{SD}}\right) + \eta_k \eta_l \right]},$$

where γ is the gyromagnetic ratio, α_k is the intrinsic Gilbert damping parameter of the $F1$ or $F2$ film, α'_k is the addition to the damping coefficient due to the spin pumping and backflow, and α''_k allows for the coupling between the two F layers due to the spin diffusion through the spacer; $M_s^{(k)}$ is the saturation magnetization of the corresponding film and Δx is the size of the computational cells along the direction normal to the interfaces. In our simulations, we solve the regular LLG equation (with $\alpha'_k = \alpha''_k = 0$) in all computational cells in F except those adjacent to F/N interfaces, for which Eq. (4) is solved. We emphasize that Eqs. (2) and (4) are valid for $F1/N/F2$ trilayers with the magnetization precession excited by *any* external stimulus, including microwave magnetic field [13] or laser pulses [27].

To model the injection of a plane elastic wave into the spin valve, we introduce a periodic displacement $\mathbf{u}(x = -t_{F1}, t) = \mathbf{u}_0(t)$ at the free surface $x = -t_{F1}$ of the $F1$ layer (Fig. 1). The surface displacement with the components $u_y^0 = u_z^0 = 0$ and $u_x^0 = u_{\max} \sin(2\pi\nu t)$ generates an oscillating strain $\varepsilon_{xx}(x, t)$ forming a longitudinal elastic wave, while a transverse wave with a shear strain $\varepsilon_{xz}(x, t)$ can be created by setting $u_x^0 = u_y^0 = 0$ and $u_z^0 = u_{\max} \sin(2\pi\nu t)$ [31,32]. The excitation frequency ν is chosen to be equal to the resonance frequency $\nu_{\text{res}}(\mathbf{H})$ of the unstrained $F1$ and $F2$ films, which is determined by simulating the relaxation of the magnetization to its equilibrium orientation at the introduced magnetic field \mathbf{H} . The amplitudes u_{\max} of the surface displacements u_x^0 and u_z^0 are given unequal values providing the same maximal strain $\varepsilon_{\max} = 10^{-4}$ in the longitudinal and shear acoustic waves having different frequencies $\nu = \nu_{\text{res}}(\mathbf{H})$ [32].

Numerical simulations are performed for $\text{Fe}_{81}\text{Ga}_{19}/\text{Au}/\text{Fe}_{81}\text{Ga}_{19}$ trilayers using the material parameters of $\text{Fe}_{81}\text{Ga}_{19}$ and Au listed in our previous paper [31]. For the reflection spin-mixing conductance of the $\text{Fe}_{81}\text{Ga}_{19}/\text{Au}$ interfaces, we employ the theoretical estimate $(e^2/h)\text{Re}[g_{\uparrow\downarrow}^r] \approx 4.66 \times 10^{14} \Omega^{-1} \text{m}^{-2}$ obtained for the Fe/Au contact [40]. Other parameters of the simulations are listed in Table I. To maximize the magnetization precession amplitude at $\text{Fe}_{81}\text{Ga}_{19}/\text{Au}$ interfaces, the thickness t_{F1} of the first $\text{Fe}_{81}\text{Ga}_{19}$ film is chosen according to the criterion derived in our previous paper for F/N bilayers (as shown in Appendix, the same criterion applies to $F1/N/F2$ trilayers). The second $\text{Fe}_{81}\text{Ga}_{19}$ film ($F2$) is given much larger thickness t_{F2} strongly exceeding the wavelength λ_F of elastic waves in galfenol. This enabled us to get rid of the elastic waves reflected from the $F2$ free surface at $x = t_N + t_{F2}$, which would have created undesired perturbation of the magnetization dynamics at the interfaces. The thickness t_N of the Au layer is varied in a wide range of values from approximately 20 nm to approximately λ_N in order to reveal the dependence of the generated spin flow on spacer thickness (λ_N denotes the wavelength of the elastic waves in Au). The equilibrium orientations of the magnetization in $F1$ and $F2$ are chosen to maximize the magnetoelastic torque exerted on them by the strain ε_{xx} in the longitudinal elastic wave or ε_{xz} in the transverse elastic wave. At the excitation by a longitudinal wave, the torque is maximized when the magnetization is inclined at 45° to the film surfaces ($m_x = m_z$ or $m_x = -m_z$). To achieve such an orientation, we introduce a constant external magnetic field $H_x = 11831.77$ Oe, the magnitude of which is chosen to counteract the

TABLE I. Parameters of the micromagnetoelastic simulations of $\text{Fe}_{81}\text{Ga}_{19}/\text{Au}/\text{Fe}_{81}\text{Ga}_{19}$ trilayers excited by longitudinal and transverse elastic waves.

	Longitudinal wave	Transverse wave
External magnetic field	$H_x = 11831.77$ Oe	None
Excitation frequency $\nu = \nu_{\text{res}}$	2.8 GHz	5.8 GHz
Equilibrium orientation of \mathbf{m} in $F1$ (same in $F2$ in the P case)	[0.712986, 0, 0.701179]	[0, 0, 1]
Equilibrium orientation of \mathbf{m} in $F2$ in the AP case	[0.712986, 0, -0.701179]	[0, 0, -1]
Wavelength λ_F of elastic wave in $F1$ and $F2$ at ν	1628 nm	693 nm
Wavelength λ_N of elastic wave in N at ν	1128 nm	254 nm
Thickness t_{F1} of $F1$	$0.5\lambda_F$	$0.75\lambda_F$

demagnetizing field, which forces the magnetization to lie in the plane of the film. In the case of a transverse elastic wave, the torque is maximized when $m_x = \pm 1$ or $m_z = \pm 1$. In our simulations of transverse elastic waves we consider trilayers with parallel (P) and antiparallel (AP) in-plane orientations of the magnetizations in two galfenol films. The same notation P and AP is used below for the magnetic states of the trilayers traversed by longitudinal elastic waves, because in these states the magnetization in the F layers has the m_z component either of the same (P) or the opposite (AP) sign (see Table I).

Micromagnetoelastic simulations are performed with the aid of an in-house software, which solves the elastodynamic equation in $\text{Fe}_{81}\text{Ga}_{19}$ and Au films by a finite-difference technique with a midpoint derivative approximation and numerically integrates the LLG equation in $\text{Fe}_{81}\text{Ga}_{19}$ films by the projective Runge-Kutta algorithm. We employ a fixed integration step $\delta t = 100$ fs and cubic computational cells with the size $\Delta x = \Delta y = \Delta z = 2$ nm smaller than the exchange length $l_{\text{ex}} \approx 4$ nm of galfenol. The “free-surface” magnetic condition $\partial \mathbf{m} / \partial x = 0$ is imposed at both F/N interfaces, while the mechanical boundary conditions at these interfaces are satisfied automatically in our computational procedure.

III. RESULTS OF MICROMAGNETOELASTIC SIMULATIONS

The simulations of $\text{Fe}_{81}\text{Ga}_{19}/\text{Au}/\text{Fe}_{81}\text{Ga}_{19}$ trilayers show that the periodic mechanical displacement $u_0(t)$ introduced at the free surface of the first galfenol film launches a longitudinal or transverse elastic wave, which propagates across the trilayer with the respective wavelength λ_F in the $\text{Fe}_{81}\text{Ga}_{19}$ films and λ_N in the Au layer (see Table I). Due to the strong magnetoelastic coupling between strains and spins in the galfenol films [31], the elastic wave excites an inhomogeneous magnetization precession with the amplitude depending on the spatial position x . Owing to the magnetoelastic feedback, this precession generates secondary elastic waves with the amplitude 2 to 3 orders of magnitude smaller than that of the driving elastic wave. They propagate in the trilayer, but do not influence significantly the magnetization dynamics in the F layers and subsequent spin pumping into N layer. After a short transition period of several nanoseconds (exact duration depends on t_N), a stationary magnetization precession settles in two galfenol films, as demonstrated by Fig. 2 for the magnetizations at the $\text{Fe}_{81}\text{Ga}_{19}/\text{Au}$ interfaces.

The data on the steady-state magnetization precession at the interfaces, which are obtained from the micromagnetoelastic simulations, allowed us to calculate the spin currents \mathbf{J}_{SP} pumped into the Au layer by the dynamically strained galfenol films. Equation (2) is then used to determine the spatial distributions of the spin accumulation and spin current in the spacer. Before proceeding to present

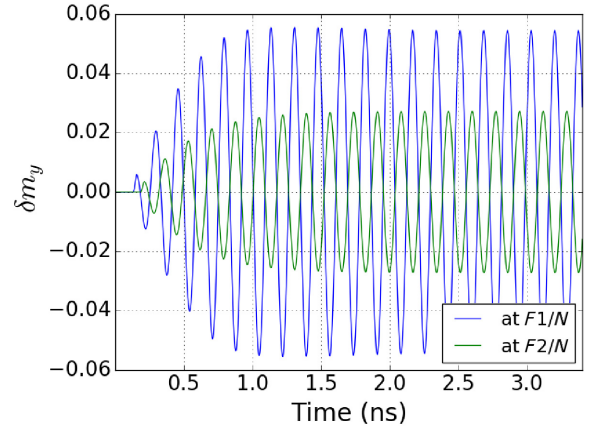


FIG. 2. Typical time dependences of magnetization precession at $F1/N$ and $F2/N$ interfaces in the $\text{Fe}_{81}\text{Ga}_{19}/\text{Au}/\text{Fe}_{81}\text{Ga}_{19}$ trilayer. Curves are plotted for parallel magnetizations in $F1$ and $F2$ layers excited by a transverse elastic wave. Spacer thickness $t_N = 80$ nm. For clarity, only the deviation of the in-plane component m_y is shown.

the results of the calculations, we briefly discuss the origin of the ac and dc parts of the pumped spin current and the parameters they depend on.

The spin-current density \mathbf{J}_{SP} can be calculated using Eq. (3) that describes its dependence on the magnetization precession at the F/N interface. For clarity, we consider small-angle precession around an equilibrium direction \mathbf{m}_0 , at which the magnetization components $m_i(t)$ can be written in a sinusoidal form $m_i = m_i^0 + \delta m_i \sin(\omega t + \varphi_{ij})$, where m_i^0 are the direction cosines of the equilibrium magnetization, δm_i are the precession amplitudes, ω is the angular frequency of the precession, and φ_{ij} is a phase shift between m_i and m_j . In this case, the nonzero components of the tensor \mathbf{J}_{SP} can be cast into a form

$$\begin{aligned} J_{xx}^{\text{SP}} &\propto m_y^0 \dot{m}_z - m_z^0 \dot{m}_y - \delta m_y \delta m_z \omega \sin(\varphi_{yz}), \\ J_{xy}^{\text{SP}} &\propto m_z^0 \dot{m}_x - m_x^0 \dot{m}_z - \delta m_x \delta m_z \omega \sin(\varphi_{zx}), \\ J_{xz}^{\text{SP}} &\propto m_x^0 \dot{m}_y - m_y^0 \dot{m}_x - \delta m_x \delta m_y \omega \sin(\varphi_{xy}). \end{aligned} \quad (5)$$

First two terms in each row of Eq. (5) correspond to ac spin current and the last term corresponds to dc spin current. Since in our simulations of the trilayers excited by a longitudinal elastic wave only $m_y^0 = 0$, all three components J_{xi}^{SP} of the ac spin current differ from zero. In contrast, the ac current generated by a shear wave has two nonzero components, because in the studied trilayers $m_x^0 = m_y^0 = 0$ yielding ac $J_{xz}^{\text{SP}} = 0$. Concerning the dc current created by a shear wave, it has only one component J_{xz}^{SP} , since at $m_z^0 = 1$ the quantity $\delta m_z = 0$ in the first approximation. In the trilayers traversed by a longitudinal wave, all three components of the dc spin current are expected to be nonzero according to Eq. (5). However, the simulations

show that $\varphi_{zx} = 180^\circ$, which nullifies the dc part of J_{xy}^{SP} . Thus, it appears that a vector having projections on the coordinate axes equal to the components J_{xi}^{SP} of the dc spin current is parallel to the equilibrium magnetization direction \mathbf{m}_0 in the F film. This interesting feature is confirmed by analytical calculations for any orientation of \mathbf{m}_0 .

Figure 3 shows representative results obtained for the spin-current densities J_{xi}^s at the $F1/N$ interface, which are calculated using Eq. (2) accounting for the spin pumping and backflow at both interfaces. Panel (a) of this figure presents the time dependences of the largest components of the ac spin current, while (b) demonstrates the evolution of the nonzero components of the dc one. It can be seen that the ac spin currents generated by longitudinal and transverse waves have similar amplitudes in the steady-state regime. In contrast, the dc spin current created by the longitudinal wave becomes 2 times larger than the one generated by the transverse wave. As it usually occurs, the ac

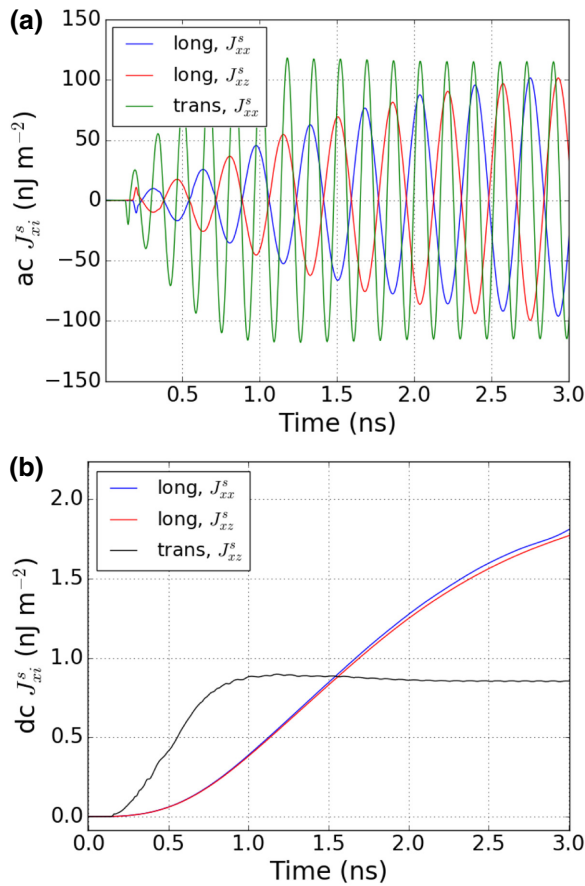


FIG. 3. Time dependences of the total spin-current densities J_{xi}^s generated at the $F1/N$ interface of the $\text{Fe}_{81}\text{Ga}_{19}/\text{Au}/\text{Fe}_{81}\text{Ga}_{19}$ trilayers traversed by longitudinal and transverse acoustic waves. Panels (a), (b) show the largest ac parts and nonzero dc parts of these spin-current densities, respectively. The magnetic states of the trilayers are assumed to be of the P type, and the Au thickness equals either 250 nm (case of longitudinal wave) or 80 nm (case of transverse one).

spin current exceeds the dc counterpart by about 2 orders of magnitude.

Let us take a closer look at the dc parts of the spin-current density \mathbf{J}_s and the spin accumulation μ_s . In our discussion, we concentrate on the components J_{xz}^s and μ_z^s , because they are present under both kinds of acoustic excitations. From Eq. (5) it follows that the pumped dc spin current J_{xz}^{SP} depends on three factors: magnetization precession amplitudes δm_x and δm_y , precession frequency ω , and the phase shift φ_{xy} between m_x and m_y . The first two factors affect the magnitude of the dc spin current, but not its sign. The last factor, however, influences both the magnitude and the sign, which has significant consequences for the total spin current in the N layer given by Eq. (2). The simulations show that $\sin \varphi_{xy}$ takes such values that the component J_{xz}^s of the dc spin current at the $F1/N$ interface has the same sign as the magnetization component m_z^0 , whereas the opposite relation holds at the $F2/N$ interface. Accordingly, the dc spin currents J_{xz}^s at the $F1/N$ and $F2/N$ interfaces are both positive or negative in the trilayers with the AP magnetic state, while they have opposite sign in the trilayers with the P state. Combining this information with Eq. (2), it can be deduced that the dc spin current J_{xz}^s in the N layer will be enhanced in the AP state and reduced in the P one with respect to the case of F/N bilayer, where the spin pumping occurs at one interface only. The opposite, however, is true for spin accumulation: the contributions to the dc part of the spin accumulation μ_z^s generated by two dynamically strained F films will add in the P state and subtract in the AP one. The above conclusions hold for the trilayers excited by both longitudinal and transverse waves, as illustrated by Fig. 4 showing the spatial distributions of the discussed quantities in the Au spacer.

Then a natural question of how the spacer thickness t_N influences the magnitudes of the spin accumulation and spin current in the Au layer arises. To quantify this influence, we calculate the total spin accumulation $\langle \mu_i^s \rangle = \int_0^{t_N} \mu_i^s(x) dx$ and the mean spin current $\langle J_{xi}^s \rangle = 1/t_N \int_0^{t_N} J_{xi}^s(x) dx$ in the spacer. Figure 5 shows the variations of the dc parts of $\langle \mu_z^s \rangle$ and $\langle J_{xz}^s \rangle$ with the spacer thickness in the $\text{Fe}_{81}\text{Ga}_{19}/\text{Au}/\text{Fe}_{81}\text{Ga}_{19}$ trilayers with the P and AP magnetic states. It can be seen that in the trilayers excited by the longitudinal elastic wave the dc part of $\langle \mu_z^s \rangle$ has strong maxima at $t_N = 0.25\lambda_N$ and $t_N = 0.75\lambda_N$ [Fig. 5(a)]. The same periodicity of $0.5\lambda_N$ between the maxima exists for the spin accumulation generated by the transverse wave, but these maxima are less pronounced and shifted to larger thicknesses $t_N \approx 0.3\lambda_N$ and $t_N \approx 0.8\lambda_N$. Regarding the average dc spin current $\langle J_{xz}^s \rangle$, it displays local maxima at $t_N \approx 0.25\lambda_N$ and $t_N \approx 0.75\lambda_N$ in the trilayers traversed by the longitudinal wave [see panel (b) in Fig. 5]. However, when excited by the transverse wave, this current decreases monotonically with increasing spacer thickness, because the trend of having local maxima

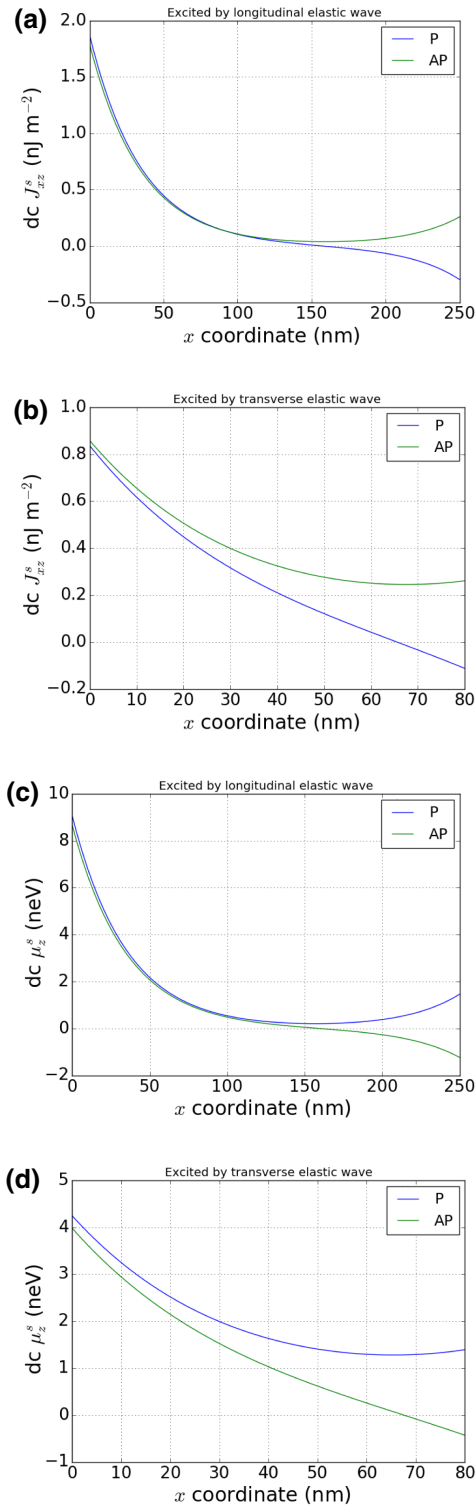


FIG. 4. Spatial distributions of the dc components of spin-current density J_{xz}^s (a), (b) and spin accumulation μ_z^s (c), (d) in Au spacers of $\text{Fe}_{81}\text{Ga}_{19}/\text{Au}/\text{Fe}_{81}\text{Ga}_{19}$ trilayers. Panels (a), (c) show the results obtained for the trilayers with the spacer thickness $t_N = 250$ nm traversed by a longitudinal elastic wave, while panels (b), (d) correspond to the trilayers with $t_N = 80$ nm excited by a transverse one. Magnetic states of the trilayers (P or AP) are indicated on the plots.

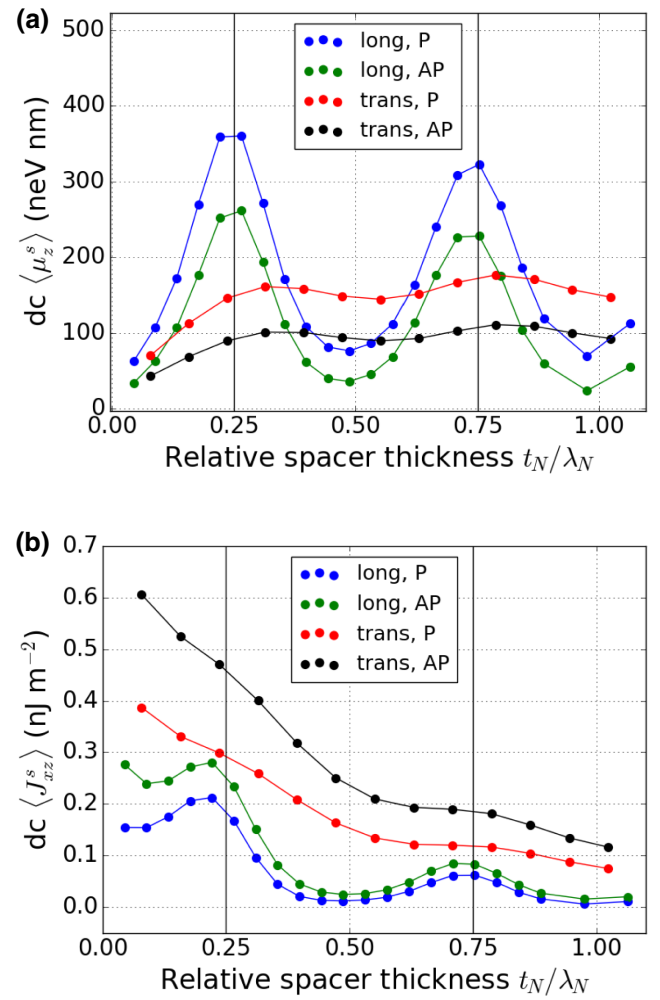


FIG. 5. Dependences of the dc parts of total spin accumulation $\langle \mu_z^s \rangle$ (a) and mean spin-current density $\langle J_{xz}^s \rangle$ (b) in the Au spacer on its thickness t_N . Data points of different colors show the results obtained for the P and AP magnetic states of the $\text{Fe}_{81}\text{Ga}_{19}/\text{Au}/\text{Fe}_{81}\text{Ga}_{19}$ trilayers excited by longitudinal and transverse elastic waves. The spacer thickness t_N is normalized by the wavelength λ_N of the respective elastic wave. Vertical lines show the spacer thicknesses providing maximal amplitudes of the acoustically induced magnetization precessions at the F/N interfaces, which are predicted by analytical calculations described in Appendix.

is suppressed by a factor of $1/t_N$ involved in the averaging. Comparing the graphs shown in Fig. 5, we find that the largest dc component of the spin accumulation $\langle \mu_z^s \rangle$ is obtained under the action of the longitudinal acoustic wave in the spin valve with the P magnetic state and Au thickness $t_N \approx 0.25\lambda_N \approx 280$ nm. In contrast, to maximize the mean dc spin current $\langle J_{xz}^s \rangle$ in the spacer, one should use the trilayer with the AP state and the smallest suitable Au thickness and choose the excitation by the transverse wave.

We also study the impact of spacer thickness on the amplitudes of the ac parts of the total spin accumulation

and mean spin current in the Au layer. These amplitudes are determined by calculating the quantities $\langle \mu_i^s \rangle$ and $\langle J_{xi}^s \rangle$ at each time moment and then evaluating the amplitudes of the resulting time-dependent functions at different values of t_N . Figure 6 shows the results obtained for the representative components of the total spin accumulation and mean spin current generated by two types of acoustic waves. It can be seen that the amplitude of the ac spin accumulation $\langle \mu_z^s \rangle$ in the trilayers excited by the longitudinal wave also has pronounced maxima at the spacer thicknesses $t_N \approx 0.25\lambda_N$ and $t_N \approx 0.75\lambda_N$. In striking contrast, the amplitude of the ac spin accumulation $\langle \mu_x^s \rangle$ generated by the transverse wave displays only one strong peak [see

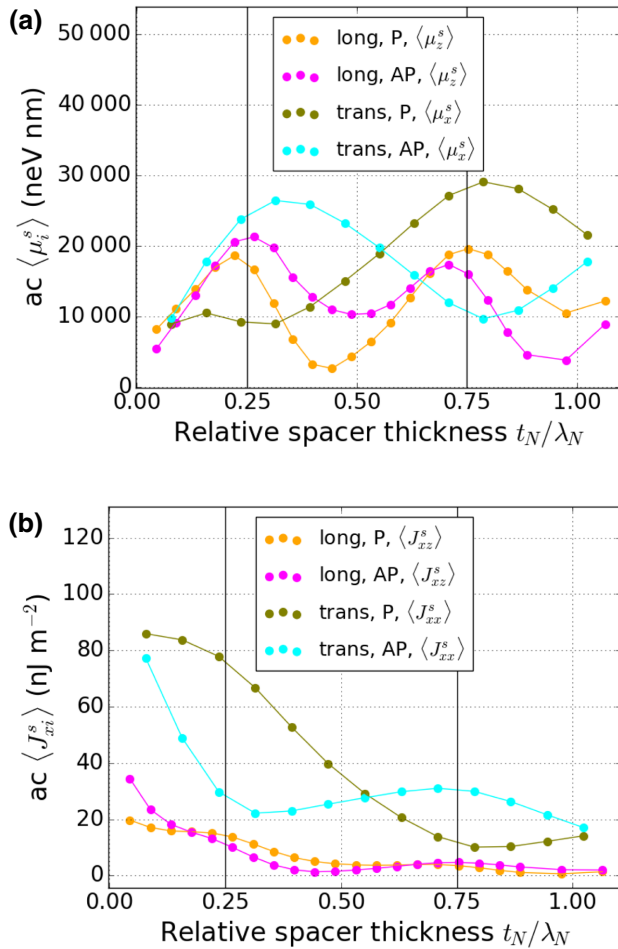


FIG. 6. Amplitudes of the ac parts of total spin accumulation $\langle \mu_i^s \rangle$ (a) and mean spin-current density $\langle J_{xi}^s \rangle$ (b) in the Au spacer plotted as a function of the spacer thickness t_N . Data points of different colors show the results obtained for the P and AP magnetic states of the $\text{Fe}_{81}\text{Ga}_{19}/\text{Au}/\text{Fe}_{81}\text{Ga}_{19}$ trilayers excited by longitudinal and transverse elastic waves. The spacer thickness t_N is normalized by the wavelength λ_N of the respective elastic wave. Vertical lines show the spacer thicknesses providing maximal amplitudes of the acoustically induced magnetization precessions at the F/N interfaces, which are predicted by analytical calculations described in Appendix.

panel (a) of Fig. 6]. Remarkably, the position of this peak depends on the magnetic state of the spin valve: the peak appears at the Au thickness $t_N \approx 0.3\lambda_N$ in the AP state and at $t_N \approx 0.8\lambda_N$ in the P one. This feature appears due to the additional factor, which affects the amplitudes of the ac parts of spin accumulation and spin current in the spacer along with those described above. Namely, these amplitudes also depend on the phase difference between the spin currents $\mathbf{J}_{\text{SP}}^{(1)}(t)$ and $\mathbf{J}_{\text{SP}}^{(2)}(t)$ generated at the $F1/N$ and $F2/N$ interfaces. This difference originates from the fact that the elastic wave needs some time to cross the N layer, which creates a phase shift of the magnetization precession at the $F2/N$ interface with respect to the precession at the $F1/N$ one. The presence of such a shift also strongly influences the mean ac spin current $\langle J_{xx}^s \rangle$ generated by the transverse acoustic wave, leading to rather different dependences of its amplitude on the spacer thickness in the trilayers with P and AP magnetic states [see panel (b) of Fig. 6]. In contrast, the magnetic state of the spin valve excited by the longitudinal elastic wave has a weak effect on the amplitude of the mean spin current $\langle J_{xz}^s \rangle$ in the Au spacer.

The most interesting result of our numerical simulations is the revealed existence of the pronounced maxima in the dependences of the total spin accumulation and mean spin current on spacer thickness. The analysis showed that this remarkable feature is caused by the enhancement of the pumped spin currents $\mathbf{J}_{\text{SP}}^{(1)}$ and $\mathbf{J}_{\text{SP}}^{(2)}$ at the spacer thicknesses $t_N \approx 0.25\lambda_N$ and $t_N \approx 0.75\lambda_N$. From Eq. (3) it follows that such an enhancement should be attributed to the increase in the magnetization precession amplitude at the interfaces. Our previous study of the magnetic dynamics in acoustically excited F/N bilayers [33] showed that the main factor governing the precession amplitude at the interface is the magnitude of the oscillating strain at that point. Therefore, we perform analytical calculations of the effect of spacer thickness on the dynamic strain states of elastic trilayers traversed by longitudinal and shear waves (see Appendix). The calculations showed that the maximal strain amplitudes at both interfaces of $F1/N/F2$ trilayers are expected at the thickness t_N^{max} given by the relation

$$t_N^{\text{max}} = \left[\frac{\arg(Q)}{\pi} + 2 - \sqrt{\alpha} \right] \frac{\lambda_N}{4} + n \frac{\lambda_N}{2}; \quad (6)$$

$$Q = \frac{c_{\alpha\alpha}^N k_N + c_{\alpha\alpha}^{F2} k_{F2}}{c_{\alpha\alpha}^N k_N - c_{\alpha\alpha}^{F2} k_{F2}},$$

where $\alpha = 1$ for longitudinal elastic wave and $\alpha = 4$ for the shear one, $n = 0, 1, 2, \dots$, $c_{\alpha\alpha}^N$ and $c_{\alpha\alpha}^{F2}$ are the elastic stiffnesses of the N and $F2$ layers, and k_N and k_{F2} are the wave numbers of the considered elastic wave in those layers. When the elastic damping is negligible, k_N and k_{F2}

can be regarded as real quantities. In this case, the parameter Q is real and $t_N^{\max} = (\lambda_N/4) + n(\lambda_N/2)$, which explains why the pumped spin currents $\mathbf{J}_{\text{SP}}^{(1)}$ and $\mathbf{J}_{\text{SP}}^{(2)}$ have maxima near such thicknesses. The total spin accumulation, which is governed by the superposition of spin currents, mostly shows similar variations with the spacer thickness, but the phase difference between $\mathbf{J}_{\text{SP}}^{(1)}(t)$ and $\mathbf{J}_{\text{SP}}^{(2)}(t)$ may eliminate one of the two maxima expected at $t_N < \lambda_N$. The same is true for the mean spin current $\langle J_{xi}^s \rangle$ in the N spacer; however, maxima at $t_N = 0.25\lambda_N$ and $0.75\lambda_N$ may get masked by a factor of $1/t_N$ involved in the averaging.

Our analytical calculations also predict an optimal thickness of the $F1$ film in the trilayer, which maximizes the strain amplitude at the $F1/N$ interface (see Appendix). They show that such a thickness depends on the value of the dimensionless parameter $Z_\alpha = \sqrt{c_{\alpha\alpha}^N \rho_N / (c_{\alpha\alpha}^{F1} \rho_{F1})}$, where ρ_N and ρ_{F1} are the mass densities of the N and $F1$ layers. Namely, when $Z_\alpha < 1$, the strain amplitude will be maximized at $t_{F1} = \lambda_{F1}/4 + n\lambda_{F1}/2$, whereas at $Z_\alpha > 1$ the optimal thickness is defined by the relation $t_{F1} = n\lambda_{F1}/2$. These results coincide with those obtained for F/N bilayers in our preceding paper [33] and, together with Eq. (6), give a recipe for choosing an optimal geometry of $F1/N/F2$ trilayers, which provides maximal amplitudes of the magnetization precessions at the $F1/N$ and $F2/N$ interfaces. The influence of the elastic damping on the optimal thicknesses of $F1$ and N layers can be taken into account by specifying the imaginary parts of the wave numbers k_{F1} , k_N , and k_{F2} . This approach is valid for materials where the decay length of acoustic wave is of the order or greater than its wavelength.

Finally, the simulations show that the long-range dynamic interaction between $F1$ and $F2$ layers, which results from the spin flow across the N spacer, does not affect the acoustically excited magnetization dynamics in any significant way. This interaction is taken into account in Eq. (4) by the terms proportional to the parameter α_k'' , but they turned out to be negligibly small in comparison with other terms.

IV. CONCLUSION

In this paper, we theoretically describe the spin dynamics generated in $\text{Fe}_{81}\text{Ga}_{19}/\text{Au}/\text{Fe}_{81}\text{Ga}_{19}$ trilayers by the injected longitudinal and transverse elastic waves. By solving the spin-diffusion equation, we derive the analytical relations for spin accumulation and spin current in the spacer, which account for the spin pumping created by the magnetization precession at the two interfaces and the spin backflow [Eq. (2)]. These relations, which are valid for any type of external stimulus exciting the magnetization precession, enable us to obtain a modified LLG equation correctly describing the local changes in the magnetic damping at the interfaces caused by spin flow in the spacer [Eq. (4)]. This equation is solved numerically together

with the elastodynamic equation in the simulations of the injection of elastic waves into the trilayer.

The numerical data on the acoustically induced stationary magnetization precession at the interfaces of the $\text{Fe}_{81}\text{Ga}_{19}/\text{Au}/\text{Fe}_{81}\text{Ga}_{19}$ trilayers are used to calculate the time dependences and spatial distributions of the spin accumulation $\mu_s(x, t)$ and spin-current density $\mathbf{J}_s(x, t)$ in the Au spacer with thickness t_N ranging from 20 nm to the wavelength λ_N of the driving elastic wave in Au. Then the ac and dc parts are determined for the projections of the vector μ_s on the coordinate axes and the nonzero components J_{xi}^s of the tensor \mathbf{J}_s . It is found that the ac parts of these quantities are generally much larger than the dc ones, with the exception of the spin-current density J_{xz}^s generated by the transverse elastic wave, which has no ac part in the geometry of our setup. In order to reveal the effects of the initial magnetization orientations in the galfenol films, we studied the trilayers with parallel and antiparallel magnetic states (see Table I in Sec. II for the definition of these states). The calculations show that the initial magnetic state of the $\text{Fe}_{81}\text{Ga}_{19}/\text{Au}/\text{Fe}_{81}\text{Ga}_{19}$ trilayer may strongly influence both the spin accumulation and spin current in the Au spacer. In particular, the dc part of the spin accumulation μ_z^s is larger in the P state than in the AP one, whereas the opposite holds for the dc spin-current density J_{xz}^s .

The most interesting results have been obtained for the impact of the spacer thickness t_N on the magnitude of acoustically generated spin imbalance in the Au layer. The simulations show that the spin currents $\mathbf{J}_{\text{SP}}^{(1)}(t)$ and $\mathbf{J}_{\text{SP}}^{(2)}(t)$ pumped at $F1/N$ and $F2/N$ interfaces have pronounced maxima at spacer thicknesses equal to about 0.25 and 0.75 of the wavelength λ_N of the elastic wave in Au, which is explained by the increase in the amplitude of the strain-induced magnetization precession (see Appendix). This feature most clearly manifests itself in the variations of the dc part of the total spin accumulation $\langle \mu_z^s \rangle$ generated by both longitudinal and transverse elastic waves [Fig. 5(a)] and of the ac part of $\langle \mu_z^s \rangle$ created by the longitudinal wave [Fig. 6(a)]. However, in the trilayers excited by the transverse wave, the ac part of $\langle \mu_x^s \rangle$ has only one pronounced maximum, which corresponds to $t_N \approx 0.3\lambda_N$ in the AP state and to $t_N \approx 0.8\lambda_N$ in the P one. In contrast, the ac and dc parts of the mean spin-current densities $\langle J_{xz}^s \rangle$ mostly become maximal at the smallest considered thicknesses of the Au spacer because the averaging involves an additional prefactor $1/t_N$ [see Figs. 5(b) and 6(b)].

Our main theoretical predictions should be valid for spin-valve structures made of other ferromagnetic and ferrimagnetic materials with strong magnetoelastic coupling and normal conductors having weak spin-flip scattering. Suitable magnetic materials include Ni, Co-Fe, and Fe-Ga alloys, and ferrimagnetic insulator CoFe_2O_4 , which have magnetoelastic constants of the order of 10^8 erg cm^{-3} [32]. The spacer can be made of a normal metal with a considerable spin-diffusion length λ_{SD} at room temperature,

such as Ag, Al, and Cu ($\lambda_{SD} = 150 - 400$ nm [41]), or a nonmagnetic semiconductor like GaAs ($\lambda_{SD} = 2.3$ μm [42]), ZnSe ($\lambda_{SD} = 1.2$ μm [43]), and GaN ($\lambda_{SD} \approx 0.7$ μm [44]). To confirm this statement, we perform micromagnetoelastic simulations of the acoustically generated spin flow in the Ni/GaAs/Ni trilayers. The simulations, which employ the set of material parameters of Ni and GaAs listed in our preceding paper [33], showed that the longitudinal and transverse elastic waves with the frequency $\nu = \nu_{\text{res}}(H_x = 1000 \text{ Oe}) \approx 3.3$ GHz efficiently generate the spin imbalance in the GaAs spacer. In similarity with the results obtained for the $\text{Fe}_{81}\text{Ga}_{19}/\text{Au}/\text{Fe}_{81}\text{Ga}_{19}$ trilayers, the spin currents pumped into GaAs at the Ni/GaAs interfaces have pronounced maxima at spacer thicknesses t_N equal to about 0.25 and 0.75 of the wavelength λ_N of the elastic wave in GaAs. However, since such thicknesses $t_N < 1$ μm are much smaller than the spin-diffusion length $\lambda_{SD} = 2.3$ μm of GaAs, the variation of spin accumulation across the GaAs spacer with $t_N < \lambda_N$ appears to be almost linear and nowhere goes to zero, which is advantageous for device applications. Furthermore, the simulations showed that the dc and ac components of the mean spin accumulation in the spacer attain maximal values at certain GaAs thicknesses, which are mostly close to either 0.25 or 0.75 of λ_N .

The results obtained in this work provide guidelines for the development and optimization of acoustically driven spin injectors into normal metals and semiconductors. The main advantage of such devices is a much lower power consumption in comparison with the conventional injectors that employ a microwave magnetic field. Indeed, the input electric power of the piezoelectric transducer, which generates an acoustic wave with a moderate strain amplitude $\varepsilon_{\text{max}} = 10^{-4}$, is predicted to be 5–10 times smaller [33] than the power consumption of a spin injector driven by the microwave magnetic field [45]. Furthermore, we reveal that the efficiency of the acoustic spin injector employing a spin-valve structure can be strongly increased via an optimal design, which takes into account the predicted variations of the generated spin signal with the spacer thickness, initial magnetic state of the $F1/N/F2$ trilayer, and the type of elastic wave used for the excitation of the magnetization precession in the ferromagnetic layers. In particular, the simulations show that the total spin accumulation in the spacer can exhibit a maximum at a certain spacer thickness, which does not happen under microwave excitation [27,28]. Another advantage of the acoustic spin injector is the electrical control of the spin accumulation magnitude, which can be easily tuned and modulated by changing the amplitude of the applied ac voltage.

The development of efficient spin injectors is useful for the realization of other spintronic devices [46–49]. For example, the functioning of spin light-emitting diodes and spin lasers creating circularly polarized light requires the creation of a spin imbalance in the active semiconductor

region, where the recombination of electrons and holes leads to the emission of light of positive and negative helicity [46,49]. Such an imbalance can be generated electrically by an integrated spin injector providing the spin flow into the gain region. As the acoustic spin injector can create a spin-polarized electric current, it also has potential applications in spin field-effect transistors (spin FETs). Indeed, the operation of a spin FET is based on changing the electric current in the channel by modulating the spin-flow characteristics, which can be achieved with the aid of a gate voltage, external magnetic field, or circularly polarized light [48]. Since reprogrammable logic operations at room temperature can be performed using the spin accumulation in a semiconductor layer [50], the acoustic spin injector is capable of facilitating an energy-efficient functioning of spin-based logic gates as well.

APPENDIX: DISTRIBUTION OF DYNAMIC STRAINS IN THE $F1/N/F2$ TRILAYER

The problem discussed here is similar to that considered in Ref. [33] but with three layers instead of two. We consider an elastic trilayer excited by a piezoelectric transducer at the boundary of one of the layers and seek for strain everywhere in the trilayer as a function of time and coordinate x (see Fig. 1 for geometry). The action of the transducer attached to the $F1$ layer is modeled by setting a boundary condition $u_i = u_i^{\text{max}} e^{-i\omega t}$ at $x = -t_{F1}$ ($i = x$ for longitudinal wave and $i = z$ for transverse one), where \mathbf{u} is the elastic displacement, u_i^{max} is the initial displacement amplitude, and t is the time (t_{F1} is the thickness of the $F1$ layer). The ansatz of plane waves is used for the mechanical displacement in the layers $F1$, N and $F2$:

$$\begin{aligned} u_i^{F1}(x, t) &= A_{F1} e^{i(k_{F1}x - \omega t)} + B_{F1} e^{-i(k_{F1}x + \omega t)}; \\ u_i^N(x, t) &= A_N e^{i(k_N x - \omega t)} + B_N e^{-i(k_N x + \omega t)}; \\ u_i^{F2}(x, t) &= A_{F2} e^{i(k_{F2}x - \omega t)}, \end{aligned} \quad (\text{A1})$$

where $A_{F1}, B_{F1}, A_N, B_N, A_{F2}$ are the (undetermined) constants and k_{F1}, k_N, k_{F2} are the wave numbers in the respective layers. We note that all of the mentioned quantities are, in the general case, complex, which simplifies the mathematical work and allows for an easy account of elastic damping by explicitly specifying the imaginary part of the wave number in the desired layer. The developed formalism works for both longitudinal and transverse elastic waves with the right choice of the elastic constants and the formula connecting the elastic displacement and strain.

The five unknown constants in Eq. (A1) require five equations to be determined. These equations come from five boundary conditions: the continuity of mechanical displacement and stress at $x = 0$, the continuity of mechanical displacement and stress at $x = t_N$ and the already mentioned action of the transducer at $x = -t_{F1}$. The $F2$ layer

is assumed either infinite or having a strong elastic damping, so we consider only elastic waves propagating away from the transducer and neglect the reflections from the $F2$ free boundary. The resulting system of equations takes the form:

$$\begin{aligned} A_{F1}F_1^- + B_{F1}F_1^+ &= u_{\max}; \\ A_{F1} + B_{F1} &= A_N + B_N; \\ c_{\alpha\alpha}^{F1}k_{F1}[A_{F1} - B_{F1}] &= c_{\alpha\alpha}^N k_N [A_N - B_N]; \\ A_N N^+ + B_N N^- &= A_{F2}F_2^+; \\ c_{\alpha\alpha}^N k_N [A_N N^+ - B_N N^-] &= c_{\alpha\alpha}^{F2} k_{F2} A_{F2} F_2^+, \end{aligned} \quad (\text{A2})$$

where

$$\begin{aligned} F_1^+ &= e^{ik_{F1}t_{F1}}, F_1^- = e^{-ik_{F1}t_{F1}}, \\ N^+ &= e^{ik_N t_N}, N^- = e^{-ik_N t_N}, \\ F_2^+ &= e^{ik_{F2}t_N} \end{aligned}$$

and $c_{\alpha\alpha}^{F1}$, $c_{\alpha\alpha}^N$, and $c_{\alpha\alpha}^{F2}$ are the elastic stiffnesses of the layers $F1$, N , and $F2$, where $\alpha = 1$ corresponds to the longitudinal elastic wave and $\alpha = 4$ to the transverse one. By solving the system, Eq. (A2), one can find all five unknown constants, and by substituting them back to Eq. (A1) obtain the sought relations for the elastic displacement in all three layers of the trilayer. The relations for strain follow immediately by differentiating the displacement with respect to x : $\varepsilon_{xx}(x, t) = \partial u_x(x, t)/\partial x$; $\varepsilon_{xz}(x, t) = (1/2)\partial u_z(x, t)/\partial x$ (we do not write explicit formulas for strain here because they are quite cumbersome). Note that the difference of $1/2$ is also present in the formulas connecting the initial strain and displacement: $u_x^{\max} = \varepsilon_{xx}^{\max}/k_{F1}$; $u_z^{\max} = 2\varepsilon_{xz}^{\max}/k_{F1}$.

Once the elastic strain $\varepsilon_{xi}(x, t)$ is known everywhere in the trilayer, we can analyze its dependence on the thicknesses of the comprising layers. In our previous work [33] we discovered that the strain amplitude at the interface between F and N layers in a bilayer is maximized when $t_F = n\lambda_F/2$ or when $t_F = \lambda_F/4 + n\lambda_F/2$ depending on a single parameter $Z_\alpha = \sqrt{c_{\alpha\alpha}^N \rho_N / (c_{\alpha\alpha}^F \rho_F)}$ being greater or smaller than unity (where ρ_F and ρ_N are the densities of the F and N layers, respectively, and λ_F is the wavelength in F). In our case there are three layers instead of two, and the conditions that maximize the strain amplitude at the $F1/N$ and $F2/N$ interfaces may, in general case, differ and depend both on t_{F1} and t_N (remember that t_{F2} will not enter the expression because we disregard the waves reflected from the free boundary of the $F2$ layer). The calculations show that it is indeed the case; however, certain simple results can be obtained under the assumption of small elastic damping in the layers ($L_{\text{dec}} \gtrsim \lambda$, L_{dec} and λ being the decay length and the wavelength in the $F1$, N , or $F2$ layer). First, the same parameter Z_α defined in the case of a trilayer as $Z_\alpha = \sqrt{c_{\alpha\alpha}^N \rho_N / (c_{\alpha\alpha}^{F1} \rho_{F1})}$ plays a significant role. When

$Z_\alpha < 1$ (transverse waves in our setup), the strain amplitude at $F1/N$ interface is independent on t_N and very close to its maximum at $t_{F1} = \lambda_{F1}/4 + n\lambda_{F1}/2$, and the strain amplitude at $F2/N$ attains its maximum at $t_{F1} = \lambda_{F1}/4 + n\lambda_{F1}/2$. Therefore, the choice of $t_{F1} = \lambda_{F1}/4 + n\lambda_{F1}/2$ seems reasonable for $Z_\alpha < 1$. When $Z_\alpha > 1$, which corresponds to the case of longitudinal elastic waves in our trilayer, the maximal strain amplitude at both interfaces can be expected at $t_{F1} = n\lambda_{F1}/2$ (λ_{F1} is the wavelength in the $F1$ layer). Once t_{F1} is fixed, the positions of the maxima of strain amplitude at both interfaces versus spacer thickness t_N can be calculated using the formula

$$\begin{aligned} t_N^{\max} &= \left[\frac{\arg(Q)}{\pi} + 2 - \sqrt{\alpha} \right] \frac{\lambda_N}{4} + n \frac{\lambda_N}{2}; \\ Q &= \frac{c_{\alpha\alpha}^N k_N + c_{\alpha\alpha}^{F2} k_{F2}}{c_{\alpha\alpha}^N k_N - c_{\alpha\alpha}^{F2} k_{F2}}. \end{aligned} \quad (\text{A3})$$

It should be noted that the predicted maximization of dynamic strains results from the optimal constructive interference of the injected wave with the waves reflected from the $F1/N$ and $N/F2$ boundaries. However, if the elastic damping in any of the layers is strong ($L_{\text{dec}} \ll \lambda$), the global maxima of the strain amplitudes at $F1/N$ and $F2/N$ interfaces may be attained at different values of t_{F1} and t_N than discussed above. In that case the corresponding values should be determined using the full expression for strain derived by solving the system, Eq. (A2), for a particular set of material parameters of the layers including their elastic damping.

-
- [1] M. N. Baibich, J. M. Broto, A. Fert, F. N. Van Dau, F. Petroff, P. Etienne, G. Creuzet, A. Friederich, and J. Chazelas, Giant Magnetoresistance of (001)Fe/(001)Cr Magnetic Superlattices, *Phys. Rev. Lett.* **61**, 2472 (1988).
 - [2] G. Binasch, P. Grünberg, F. Saurenbach, and W. Zinn, Enhanced magnetoresistance in layered magnetic structures with antiferromagnetic interlayer exchange, *Phys. Rev. B* **39**, 4828 (1989).
 - [3] D. Heim, R. Fontana, C. Tsang, V. Speriosu, B. Gurney, and M. Williams, Design and operation of spin valve sensors, *IEEE Trans. Magn.* **30**, 316 (1994).
 - [4] J. Daughton, J. Brown, E. Chen, R. Beech, A. Pohm, and W. Kude, Magnetic field sensors using GMR multilayer, *IEEE Trans. Magn.* **30**, 4608 (1994).
 - [5] C. Tsang, R. Fontana, T. Lin, D. Heim, V. Speriosu, B. Gurney, and M. Williams, Design, fabrication and testing of spin-valve read heads for high density recording, *IEEE Trans. Magn.* **30**, 3801 (1994).
 - [6] E. M. Williams, *Design and Analysis of Magnetoresistive Recording Heads* (Wiley, New York, 2001).
 - [7] B. Prince, *Emerging Memories-Technologies and Trends* (Kluwer, Norwell, MA, 2002).

- [8] C. Cavaco, M. van Kampen, L. Lagae, and G. Borghs, A room-temperature electrical field-controlled magnetic memory cell, *J. Mater. Res.* **22**, 2111 (2007).
- [9] N. A. Pertsev and H. Kohlstedt, Resistive switching via the converse magnetoelectric effect in ferromagnetic multilayers on ferroelectric substrates, *Nanotechnology* **21**, 475202 (2010).
- [10] J.-R. Chen, A. Smith, E. A. Montoya, J. G. Lu, and I. N. Krivorotov, Spin-orbit torque nano-oscillator with giant magnetoresistance readout, *Commun. Phys.* **3**, 187 (2020).
- [11] P. Bruno, and C. Chappert, Oscillatory Coupling between Ferromagnetic Layers Separated by a Nonmagnetic Metal Spacer, *Phys. Rev. Lett.* **67**, 1602 (1991).
- [12] Z. Celinski and B. Heinrich, Exchange coupling in Fe/Cu, Pd, Ag, Au/Fe trilayers, *J. Magn. Magn. Mater.* **99**, L25 (1991).
- [13] B. Heinrich, Y. Tserkovnyak, G. Woltersdorf, A. Brataas, R. Urban, and G. E. W. Bauer, Dynamic Exchange Coupling in Magnetic Bilayers, *Phys. Rev. Lett.* **90**, 187601 (2003).
- [14] Y. Tserkovnyak, A. Brataas, G. E. W. Bauer, and B. I. Halperin, Nonlocal magnetization dynamics in ferromagnetic heterostructures, *Rev. Mod. Phys.* **77**, 1375 (2005).
- [15] A. Kirilyuk, A. V. Kimel, and T. Rasing, Ultrafast optical manipulation of magnetic order, *Rev. Mod. Phys.* **82**, 2731 (2010).
- [16] K. Uchida, H. Adachi, T. An, T. Ota, M. Toda, B. Hillebrands, S. Maekawa, and E. Saitoh, Long-range spin Seebeck effect and acoustic spin pumping, *Nat. Mater.* **10**, 737 (2011).
- [17] M. Weiler, L. Dreher, C. Heeg, H. Huebl, R. Gross, M. S. Brandt, and S. T. B. Goennenwein, Elastically Driven Ferromagnetic Resonance in Nickel Thin Films, *Phys. Rev. Lett.* **106**, 117601 (2011).
- [18] A. V. Scherbakov, A. S. Salasyuk, A. V. Akimov, X. Liu, M. Bombeck, C. Brüggemann, D. R. Yakovlev, V. F. Sapega, J. K. Furdyna, and M. Bayer, Coherent Magnetization Precession in Ferromagnetic (Ga, Mn)As Induced by Picosecond Acoustic Pulses, *Phys. Rev. Lett.* **105**, 117204 (2010).
- [19] A. V. Azovtsev and N. A. Pertsev, Excitation of high-frequency magnon modes in magnetoelastic films by short strain pulses, *Phys. Rev. Mater.* **4**, 064418 (2020).
- [20] L. Thevenard, C. Gourdon, J. Y. Prieur, H. J. von Bardeleben, S. Vincent, L. Becerra, L. Largeau, and J.-Y. Duquesne, Surface-acoustic-wave-driven ferromagnetic resonance in (Ga, Mn)(As, P) epilayers, *Phys. Rev. B* **90**, 094401 (2014).
- [21] S. G. Alekseev, S. E. Dizhur, N. I. Polzikova, V. A. Luzanov, A. O. Raevskiy, A. P. Orlov, V. A. Kotov, and S. A. Nikitov, Magnons parametric pumping in bulk acoustic waves resonator, *Appl. Phys. Lett.* **117**, 072408 (2020).
- [22] S. I. Kiselev, J. C. Sankey, I. N. Krivorotov, N. C. Emley, R. J. Schoelkopf, R. A. Buhrman, and D. C. Ralph, Microwave oscillations of a nanomagnet driven by a spin-polarized current, *Nature* **425**, 380 (2003).
- [23] W. H. Rippard, M. R. Puffall, S. Kaka, S. E. Russek, and T. J. Silva, Direct-Current Induced Dynamics in $\text{Co}_{90}\text{Fe}_{10}/\text{Ni}_{80}\text{Fe}_{20}$ Point Contacts, *Phys. Rev. Lett.* **92**, 027201 (2004).
- [24] T. Nozaki, Y. Shiota, S. Miwa, S. Murakami, F. Bonell, S. Ishibashi, H. Kubota, K. Yakushiji, T. Saruya, A. Fukushima, S. Yuasa, T. Shinjo, and Y. Suzuki, Electric-field-induced ferromagnetic resonance excitation in an ultrathin ferromagnetic metal layer, *Nat. Phys.* **8**, 491 (2012).
- [25] J. Zhu, J. A. Katine, G. E. Rowlands, Y.-J. Chen, Z. Duan, J. G. Alzate, P. Upadhyaya, J. Langer, P. K. Amiri, K. L. Wang, and I. N. Krivorotov, Voltage-Induced Ferromagnetic Resonance in Magnetic Tunnel Junctions, *Phys. Rev. Lett.* **108**, 197203 (2012).
- [26] G. Viaud and N. A. Pertsev, Dynamic converse magnetoelectric effect in ferromagnetic nanostructures with electric-field-dependent interfacial anisotropy, *Phys. Rev. B* **90**, 064429 (2014).
- [27] A. P. Danilov, A. V. Scherbakov, B. A. Glavin, T. L. Linnik, A. M. Kalashnikova, L. A. Shelukhin, D. P. Pattnaik, A. W. Rushforth, C. J. Love, S. A. Cavill, D. R. Yakovlev, and M. Bayer, Optically excited spin pumping mediating collective magnetization dynamics in a spin valve structure, *Phys. Rev. B* **98**, 060406 (2018).
- [28] X. Joyeux, T. Devolder, J.-V. Kim, Y. Gomez de la Torre, S. Eimer, and C. Chappert, Configuration and temperature dependence of magnetic damping in spin valves, *J. Appl. Phys.* **110**, 063915 (2011).
- [29] H. Yang, Y. Li, and W. E. Bailey, Large spin pumping effect in antisymmetric precession of $\text{Ni}_{79}\text{Fe}_{21}/\text{Ru}/\text{Ni}_{79}\text{Fe}_{21}$, *Appl. Phys. Lett.* **108**, 242404 (2016).
- [30] S. Takahashi, Giant enhancement of spin pumping in the out-of-phase precession mode, *Appl. Phys. Lett.* **104**, 052407 (2014).
- [31] A. V. Azovtsev and N. A. Pertsev, Coupled magnetic and elastic dynamics generated by a shear wave propagating in ferromagnetic heterostructure, *Appl. Phys. Lett.* **111**, 222403 (2017).
- [32] A. V. Azovtsev and N. A. Pertsev, Dynamical spin phenomena generated by longitudinal elastic waves traversing CoFe_2O_4 films and heterostructures, *Phys. Rev. B* **100**, 224405 (2019).
- [33] A. V. Azovtsev, A. I. Nikitchenko, and N. A. Pertsev, Energy-efficient spin injector into semiconductors driven by elastic waves, *Phys. Rev. Mater.* **5**, 054601 (2021).
- [34] A. V. Azovtsev and N. A. Pertsev, Magnetization dynamics and spin pumping induced by standing elastic waves, *Phys. Rev. B* **94**, 184401 (2016).
- [35] M. D. Stiles and A. Zangwill, Anatomy of spin-transfer torque, *Phys. Rev. B* **66**, 014407 (2002).
- [36] Y. Tserkovnyak and A. Brataas, Spin pumping and magnetization dynamics in metallic multilayers, *Phys. Rev. B* **66**, 224403 (2002).
- [37] O. Mosendz, J. E. Pearson, F. Y. Fradin, G. E. W. Bauer, S. D. Bader, and A. Hoffmann, Quantifying Spin Hall Angles from Spin Pumping: Experiments and Theory, *Phys. Rev. Lett.* **104**, 046601 (2010).
- [38] M. I. Dyakonov and V. I. Perel, Current-induced spin orientation of electrons in semiconductors, *Phys. Lett. A* **35**, 459 (1971).
- [39] Y. Tserkovnyak, A. Brataas, and G. E. W. Bauer, Enhanced Gilbert Damping in Thin Ferromagnetic Films, *Phys. Rev. Lett.* **88**, 117601 (2002).

- [40] M. Zwierzycki, Y. Tserkovnyak, P. J. Kelly, A. Brataas, and G. E. W. Bauer, First-principles study of magnetization relaxation enhancement and spin transfer in thin magnetic films, *Phys. Rev. B* **71**, 064420 (2005).
- [41] J. Bass and W. P. Pratt, Spin-diffusion lengths in metals and alloys, and spin-flipping at metal/metal interfaces: An experimentalist's critical review, *J. Phys.: Condens. Matter* **19**, 183201 (2007).
- [42] J. M. Kikkawa and D. D. Awschalom, Resonant Spin Amplification in n-Type GaAs, *Phys. Rev. Lett.* **80**, 4313 (1998).
- [43] M. E. Flatté and I. Tifrea, eds., *Manipulating Quantum Coherence in Solid State Systems* (Springer, Dordrech, 2007), Vol. 244.
- [44] T.-E. Park, Y. H. Park, J.-M. Lee, S. W. Kim, H. G. Park, B.-C. Min, H.-j. Kim, H. C. Koo, H.-J. Choi, S. H. Han, M. Johnson, and J. Chang, Large spin accumulation and crystallographic dependence of spin transport in single crystal gallium nitride nanowires, *Nat. Commun.* **8**, 15722 (2017).
- [45] K. Ando, S. Takahashi, J. Ieda, H. Kurebayashi, T. Trypiniotis, C. H. W. Barnes, S. Maekawa, and E. Saitoh, Electrically tunable spin injector free from the impedance mismatch problem, *Nat. Mat.* **10**, 655 (2011).
- [46] I. Žutić, J. Fabian, and S. Das Sarma, Spintronics: Fundamentals and applications, *Rev. Mod. Phys.* **76**, 323 (2004).
- [47] D. D. Awschalom and M. E. Flatté, Challenges for semiconductor spintronics, *Nat. Phys.* **3**, 153 (2007).
- [48] A. Hirohata, K. Yamada, Y. Nakatani, I.-L. Prejbeanu, B. Diény, P. Pirro, and B. Hillebrands, Review on spintronics: Principles and device applications, *J. Magn. Magn. Mater.* **509**, 166711 (2020).
- [49] I. Žutić, G. Xu, M. Lindemann, P. E. Faria Junior, J. Lee, V. Labinac, K. Stojšić, G. M. Sipahi, M. R. Hofmann, and N. C. Gerhardt, Spin-lasers: Spintronics beyond magnetoresistance, *Solid. State. Commun.* **316-317**, 113949 (2020).
- [50] H. Dery, P. Dalal, Ł. Cywiński, and L. J. Sham, Spin-based logic in semiconductors for reconfigurable large-scale circuits, *Nature* **447**, 573 (2007).